CHAPTER 1

INTRODUCTION

1.1.   Motivation for the Thesis

Integrated circuits (ICs) have experienced tremendous growth over the last six decades. During this period, the use of integrated circuits have steadily increased while their size has decreased [Moore (1998)]. The most important add-ons for ICs are signal- and power-routing layers of metals. During the first portion of chip-making, the electronic components are fabricated on a silicon wafer. In the back-end-of-line, these components are connected through metal wires to each other (to distribute signals) as well as to power sources and to the ground. These wires are known as interconnects.

The function of an interconnect is to distribute the clock and other signals and to provide power/ground, to and among, the various circuits functions on a chip [Grabinski (2000)]. In the early generations of metal-oxide-semiconductor (MOS) technology, only one or two layers were available for metallization. But the transistor density has increased tremendously, and the number of layers of interconnects has gone over ten, as shown in Fig 1.1. Interconnects close to the transistors need to be small, as they join components that are themselves very small and often closely packed together. These lower-level lines —called-local interconnects—are usually thin and short. Global interconnects are higher up in the structure; they connect different blocks of the IC and are thus typically thick, long, and widely separated. Connections between interconnect levels, called vias, allow signals and power to be transmitted from one level to the next.

The basic requirement for many interconnects is to transfer the signal/information with high speed. Electronic interconnects are ultra-tiny wires due to shrinking feature sizes. The scaling of the ICs has brought many challenges for electronic interconnects, thereby limiting IC speed [Ozbay (2006)].

Electronic interconnects are now a significant bottleneck in IC technology. For boosting the speed of semiconductor chips, a vast amount of information transfer between the transistors is required, but that cannot be sustained by electronic interconnects [Miller (2010)]. Table 1.1 highlights the limitations of electronic interconnects. Most prominent are the increases in delay time for signal propagation, power dissipation, and cross-talk amongst wires. These limitations arise by electric charging and discharging when information is being transmitted along a metal wire [Conway *et al.* (2007)].

Figure 1.1: Interconnect architecture including local and global interconnects.
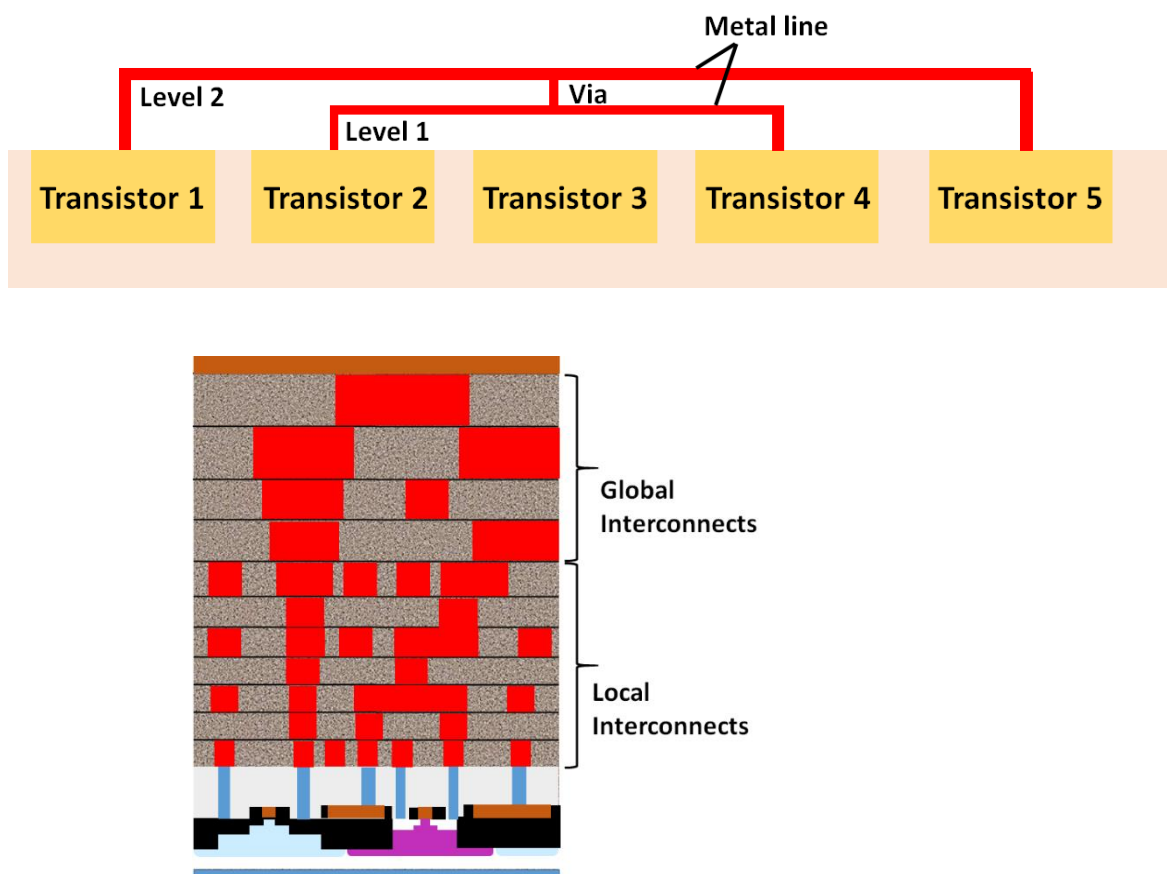
An alternative to the charging and discharging of wires for transfer of information inside ICs is to use optical interconnects. The data-transfer rate increases because photons can travel faster than electrons in a chip. However, due to the diffraction limit [Sekhon and Verma (2011)], the size of the optical interconnect must be approximately half of the

wavelength of the carrier light wave passing through it. Accordingly, the cross-sectional dimensions of a optical interconnect do not match the dimensions of electrical contacts. Therefore, optical interconnects are not as good as electronic interconnects in integration, being limited by the size-mismatch problem. Both electronic and optical interconnects provide limited data-transfer rates [Sekhon and Verma (2011)], but higher rates are needed due to miniaturization.

Table 1.1: Limitations of electronic interconnects

Limitation	Summary
Signal delay	Signal propagation is limited by the RC time constant [Conway *et al.* (2007)] of an interconnect. As the cross-section area of the wire is reduced, the wire resistance increases.
Power dissipation	As interconnect density increases through scaling, the energy dissipated per unit of chip area increases proportionally.
Crosstalk	The increase in distributed wire resistance per unit length with geometric scaling increases cross-talk amongst wires.

Electromagnetic surface waves (ESWs) guided by metal/dielectric interfaces are called surface-plasmon-polariton (SPP) waves. These surface waves are promising candidates for information transfer inside a semiconductor chip because of the strong confinement of their fields on the subwavelength-scale [Barnes *et al.* 2003]. Due to the concentration of light below the diffraction limit, SPP-wave-based optical interconnects can help bridge the size gap and also speed up the data-transfer rate [Leuthold *et al.* (2013)]. The energy required to receive and send a pulse-modulated SPP wave can be less than that needed for the electric charging of a metallic wire. This could allow information transfer from one transistor to another transistor with a high bit rate [Sekhon and Verma (2011)].

With this motivation, a state-of-the-art numerical technique is used in this thesis to investigate the propagation and scattering of pulse-modulated carrier SPP waves in an environment that represents an interconnect. The investigation is performed in the time domain by solving the time-domain Maxwell equations using the finite-difference time-domain (FDTD) method. The materials involved are characterized using well-established models such as the Lorentz and the critical-point models for dielectric materials, and the Drude model for metals. The fidelity of information transmission between the transmitted signal and the received signal is assessed by statistical techniques, which would eventually allow the determination of optimal configurations for information transfer with acceptable fidelity. Thus, the feasibility of harnessing SPP waves for information transfer inside semiconductor chips is established.

In the remainder of this chapter, the basic concepts needed for the rest of the thesis are provided. The fundamentals of ESWs and their classification based on the types of the two partnering materials are presented in Sec. 1.2. The canonical boundary-value problem of the propagation of an SPP wave guided by the planar interface of a metal and an isotropic dielectric material is formulated in the frequency domain and solved in Sec. 1.3. Typical models used for the relative permittivities of isotropic and dispersive materials are discussed in Sec. 1.4. The FDTD method used in Chapters 2-4 to compute the spatiotemporal evolution of the electromagnetic field of a pulse-modulated carrier SPP wave is presented in Sec. 1.5. In order to determine the fidelity of information transfer by the pulse-modulated carrier SPP wave, two different correlation coefficients used in the thesis are presented in Sec. 1.6. A detailed literature review of ESWs and ESW-based optical interconnects in semiconductor chips are presented in Sec. 1.7. The objective and the research tasks undertaken are provided in Sec. 1.8 and the organization of the thesis is described in Sec. 1.9.

1.2.   Electromagnetic Surface Waves

An ESW propagates guided by the interface of two different materials, as illustrated in Fig 1.2. The amplitudes of the electromagnetic fields of an ESW are usually maximum at or near the interface and decrease with the distance on both sides of the interface [Polo *et al*. (2013), Maier (2007)]. Therefore, the fields of an ESW are highly localized to the interface. This localization is a desirable quality for optical sensing [Nylander *et al*. (1982)] as well as for thin optical interconnects in semiconductor chips [Ozbay (2007), Barnes *et al.* (2003)].
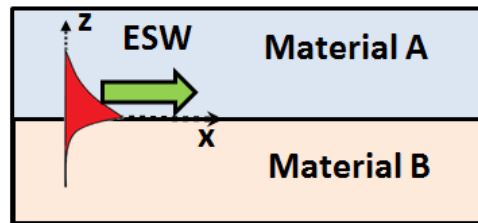

Figure 1.2: Electromagnetic surface wave guided by the interface of two different materials.

ESWs are classified depending on the two partnering materials, as shown in Table 1.2.

The **Surface-plasmon-polariton** wave is the most popularly researched ESW. Its propagation is guided by a planar metal/dielectric interface. The electromagnetic fields of the SPP wave are strongly bound to the metal/dielectric interface. The plasmon component of an SPP wave results from the collective oscillation of free electrons (plasma oscillation) on a metal surface illuminated by an external electromagnetic wave. The polariton component of an SPP wave results from the collective oscillation of atomic and molecular dipole moments in the dielectric partnering material illuminated by an external electromagnetic wave. SPP waves are classical counterparts of trains of quasiparticles called SPPs [Polo *et al*. (2013), Maier (2007)]. In this thesis, the SPP wave is used as a

carrier wave to transport information inside a semiconductor chip. Therefore, the SPP wave is discussed in more detail in Sec. 1.3.

Table 1.2: Classification of electromagnetic surface wave

Material A	Material B	Electromagnetic Surface Wave
Dielectric	Metal	Surface-plasmon-polariton wave
Homogeneous, isotropic dielectric	Homogeneous, dissipative, isotropic dielectric	Uller-Zenneck wave
Homogeneous dielectric	Homogeneous, anisotropic dielectric	Dyakonov wave
Homogeneous, isotropic dielectric	Periodically nonhomogeneous, isotropic dielectric	Tamm wave
Homogeneous, isotropic dielectric	Periodically nonhomogeneous, anisotropic dielectric	Dyakonov-Tamm wave

The **Uller-Zenneck wave** is guided by the planar interface of two homogeneous and isotropic dielectric materials, of which only one must be a dissipative material [Faryad and Lakhtakia (2014)]. The Uller-Zenneck wave is named after Uller [Uller (1903)] and Zenneck [Zenneck (1907)] who theoretically established the existence of an electromagnetic surface wave guided by the planar interface of air/seawater (dissipative) and air/ground (dissipative) respectively in the radio-frequency regime. The phase speed of the Uller-Zenneck wave is greater than that of a plane wave in either partnering material. This wave does not require any phase-matching technique for excitation, unlike SPP waves [Faryad and Lakhtakia (2014)]. The propagation distance of the Uller-Zenneck wave is in the millimeter range at optical frequencies [Faryad and Lakhtakia (2014)]; thus, it can be used for intrachip optical interconnect.

The **Dyakonov wave** is guided by the interface of two dielectric materials that differ in crystallographic symmetry [Walker *et al.* (1998), Crasovan *et al.* (2005), Takayama *et al.* (2008)]. This special type of ESW was first predicted by Marchevskii *et al.* [Marchevskii *et al.* (1984)] in 1984, but credit is usually given to a 1988 paper of D'yakonov [D'yakonov (1988)], who considered the interface of a uniaxial dielectric material and an isotropic dielectric material and showed that, under certain conditions, wave propagation can be localized to the interface. In contrast to SPP waves, Dyakonov waves can be propagated when both partnering materials are lossless; thus, in practice, Dyakonov waves can have much larger propagation distances than SPP waves, which is their most fascinating property. Dyakonov waves are highly directional, propagating in a narrow angular range of directions with respect to the optical axis of the uniaxial partnering material. Generally, Dyakonov waves are weakly localized and their angular existence domain depends on the dielectric properties of both partnering materials [Polo *et al.* (2013), Takayama *et al.* (2008)]. These waves have potential applications in integrated optics, optical sensing [Torner *et al.* (1995)], and optical waveguiding [Torner *et al.* (1993)].

The **Tamm wave** is guided by the interface of two isotropic dielectric materials when one partnering material is periodically nonhomogeneous in the direction normal to the interface. Tamm waves are named after I. Y. Tamm because he pointed out that electron states at the surface of and inside a material are different [Polo *et al.* (2013)]. The optical analog of a surface electron state is a surface wave guided by the interface of two dissimilar materials, at least one of which is periodically nonhomogeneous in the direction normal to the interface. Unlike the SPP waves, the number of modes for Tamm-wave propagation is greater than one [Maab *et al.* (2011), Polo *et al.* (2013)]. The existence of Tamm waves has been experimentally established [Yeh *et al.* (1978),

Robertson and May (1999), Robertson (1999)] and has been exploited for optical biosensing [Konopsky and Alieva (2007)]. Since both partnering materials can be weakly dissipative in nature, the propagation distance of a Tamm wave can be higher in comparison to that of an SPP wave.

A **Dyakonov-Tamm** wave is guided by the interface of two dielectric materials, of which at least one is both anisotropic and periodically nonhomogeneous in the direction normal to the interface [Polo *et al.* (2013)]. The Dyakonov-Tamm wave has a larger angular range of direction of propagation in comparison to the Dyakonov wave [Takayama *et al.* (2008), Nelatury *et al.* (2008)]. Lakhtakia *et al.* introduced periodic nonhomogeneity by using a periodic sculptured thin film (STF) as one of the two partnering dielectric materials, the other being isotropic and homogeneous and they deduced that larger angular existence domain of Dyakonov-Tamm waves is due to the periodic nonhomogeneity of either one or both partnering dielectric materials [Lakhtakia and Messier (2005), Lakhtakia (2002), Polo *et. al.* (2011)]. Agarwal *et al*. studied the propagation of the Dyakonov–Tamm waves guided by the interface of an isotropic dielectric material and a periodically nonhomogeneous sculptured nematic thin film [Agrawal *et al.* (2009)]. Gao et al. theoretically examined the propagation of Dyakonov–Tamm waves guided by a twist-defect interface in a chiral sculptured thin film [Gao *et al.* (2009)].

1.3.   Surface-Plasmon-Polariton Waves

A surface-plasmon-polariton (SPP) wave is an ESW whose propagation is guided by a metal/dielectric interface. The term "surface-plasmon-polariton" indicates that this ESW involves both a plasmonic component (in the metallic partner) and a polaritonic component (in the dielectric partner). The plasmonic component arises due to the

collective oscillations of electrons present on the naked surface of a metal when illuminated by an external electromagnetic wave. The polaritonic component results from the collective oscillations of the atomic and molecular dipole moments in a similarly illuminated dielectric material [Polo *et al.* (2013), Maier (2007)].

When air is the partnering dielectric material, the simpler term "surface-plasmon wave" is often used, because the polaritonic component is absent.

Quasiparticles called surface plasmons were predicted as self-sustained collective oscillations of electrons at metal surfaces by Ritchie [Ritchie (1957)]. It had already been pointed out by Bohm and Pines [Bohm and Gross (1949)a, Bohm and Gross (1949)b, Pines (1956)] that the Coulomb interaction between valence electrons in metals exposed to electric fields yield collective plasma oscillations similar to the electron-density oscillations predicted by Tonks and Langmuir in electrical discharges in gases [Tonk and Langmuir (1929)]. In 1959, Powell and Swan demonstrated the existence of electron-cloud oscillation in electron energy-loss experiments on aluminum [Powell and Swan (1959)a, Powell and Swan (1959)b]. Since then, there has been a significant advance in both theoretical and experimental investigations of surface plasmons. Surface-plasmon-polaritons are analogous quasiparticles that can exist on metal/dielectric interfaces.

The amplitude of the electric field of an SPP wave is maximum at or near the interface and decreases with the distance on both sides of the interface, as shown in Fig 1.3. Therefore, the electromagnetic fields of an SPP wave are highly localized to the interface over distances are in the range of present-day electronic circuit elements. Owing to stronger localization, SPP-wave-based interconnects are not restricted in size by the diffraction limit unlike standard optical interconnects (such as waveguides [Brongersma *et al.* (2007)]). Thus SPP-wave-based interconnects can guide signals at a subwavelength scale.

Furthermore, SPP waves are extremely sensitive to changes in the refractive index near the metal surface. Such a change may result in a shift in the resonant frequency of the incident light (if the direction of the incident light is fixed) [Homola *et al.* (1995)], or a change in the resonant direction of the incident light (if the frequency of the incident light is fixed) [Liedberg *et al.* (1993)]. The resonance is manifested as a sudden drop in the intensity of the reflected light [Abdulhalim *et al.* (2008)], as either the frquency or the direction of the incident light is varied. The magnitude of the resonance shift is quantitatively related to the magnitude of the change in the refractive index of the medium in contact with the metal surface. Therefore, SPP waves are commonly used for the detection of different types of materials that could be gaseous, liquid, or solid [Abdulhalim *et al.* (2008)].
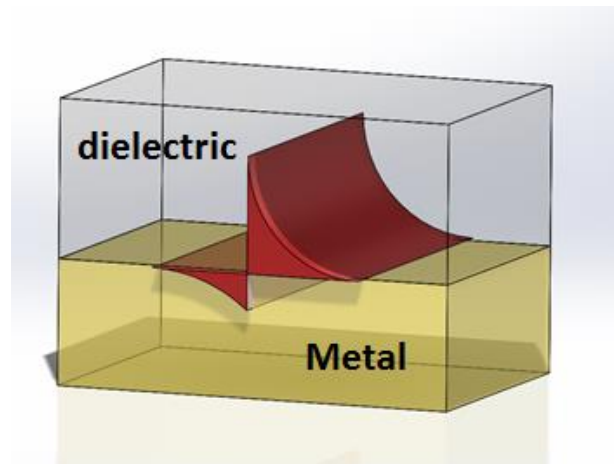

Figure 1.3: Highly localized fields of an SPP wave.

1.3.1. Fields and Dispersion Equation

Let us consider SPP wave propagation as depicted in Fig. 1.4. The half-space $z > 0$ is occupied by an isotropic and homogeneous dielectric material with relative permittivity $\tilde{\varepsilon}_d$, and the half-space $z < 0$ is occupied by an isotropic and homogeneous metal with

relative permittivity $\tilde{\varepsilon}_m$. Both $\tilde{\varepsilon}_d$ and $\tilde{\varepsilon}_m$ are functions of frequency, the SPP wave being a frequency-domain entity.

The SPP wave propagates guided by the plane $z = 0$ along the x-direction and attenuates as $z \to \pm\infty$. The polarisation of the SPP wave would be described later. Let $\mathbf{k}_d$ and $\mathbf{k}_m$ be the wavevectors in the dielectric and metal half-spaces, respectively. The wavevector in the region $z > 0$ may be written as

$$\mathbf{k}_d = q\,\hat{\mathbf{u}}_x + \alpha_d\,\hat{\mathbf{u}}_z, \tag{1.1}$$

and the wavevector in the region $z < 0$ may be written as

$$\mathbf{k}_m = q\,\hat{\mathbf{u}}_x - \alpha_m\,\hat{\mathbf{u}}_z, \tag{1.2}$$

where q, α_d, and α_m are complex-valued, and $\hat{\mathbf{u}}_x$ and $\hat{\mathbf{u}}_z$ are the Cartesian unit vectors. Although the wavevectors $\mathbf{k}_d$ and $\mathbf{k}_m$ are different, their components along the propagation direction are the same. This is the necessary condition in order to satisfy the boundary conditions across the interface z = 0 [Chen (1983)].
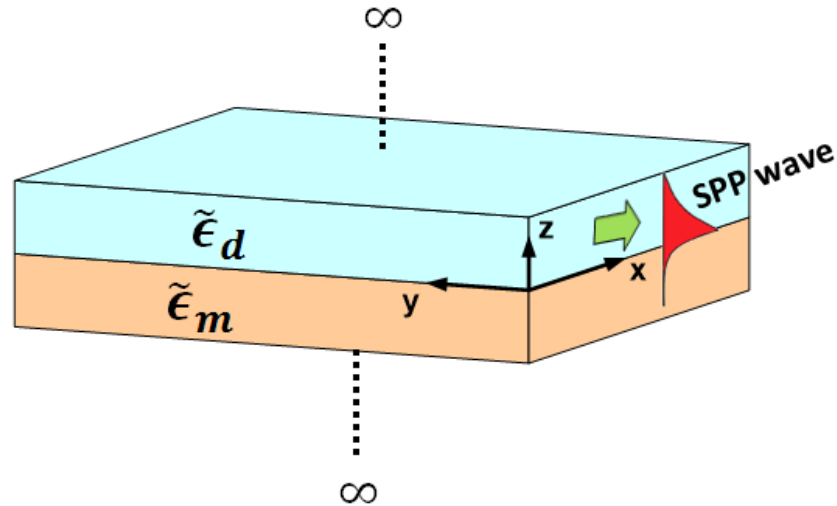

Figure 1.4: Geometry for SPP wave propagation.

In order for the SPP wave to be bound to the interface $z = 0$, the z-directed components of the wavevectors $\mathbf{k}_d$ and $\mathbf{k}_m$ must be complex-valued with non-zero

imaginary parts. For the SPP wave to be localized to the interface and decay as $z \to \pm\infty$, the following conditions must be satisfied:

$$\left.\begin{array}{c} \mathrm{Im}(\alpha_d) > 0 \\ \mathrm{Im}(\alpha_m) > 0 \end{array}\right\}. \tag{1.3}$$

The full set of the frequency-domain Maxwell equations in the absence of external sources can be expressed as follows [Chen (1983)]:

$$\left.\begin{array}{c} \nabla \times \tilde{\mathbf{E}} = i\omega \tilde{\mathbf{B}} \\ \nabla \times \tilde{\mathbf{H}} = -i\omega \tilde{\mathbf{D}} \\ \nabla \cdot \tilde{\mathbf{D}} = 0 \\ \nabla \cdot \tilde{\mathbf{B}} = 0 \end{array}\right\}, \tag{1.4}$$

where the phasors $\tilde{\mathbf{E}}$, $\tilde{\mathbf{H}}$, $\tilde{\mathbf{D}}$, and $\tilde{\mathbf{B}}$ represent the electric field, magnetic field, dielectric displacement, and magnetic flux density, respectively. An $\exp(-i\omega t)$ dependence on time t is implicit with $i = \sqrt{-1}$ and ω as the angular frequency. The frequency-domain constitutive relations for a linear, isotropic and nonmagnetic medium are

$$\tilde{\mathbf{H}} = \mu_0^{-1} \tilde{\mathbf{B}}, \qquad\qquad \tilde{\mathbf{D}} = \varepsilon_0 \tilde{\varepsilon}_r \tilde{\mathbf{E}}, \tag{1.5}$$

where $\mu_0 \left(= 4\pi \times 10^{-7}\,\mathrm{H/m}\right)$ and $\varepsilon_0 \left(= 8.854 \times 10^{-12}\,\mathrm{F/m}\right)$ are the permeability and permittivity of free space, respectively, and $\tilde{\varepsilon}_r$ is the relative permittivity of the medium.

The simplest solution to Eqs. (1.4) is a plane wave [Mackay and Lakhtakia (2019)]. The fields phasors of the plane wave can be written as [Polo *et al.* (2013)]

$$\tilde{\mathbf{E}}(r) = M \exp(i\mathbf{k} \cdot \mathbf{r}) \tag{1.6}$$

$$\tilde{\mathbf{H}}(r) = N \exp(i\mathbf{k} \cdot \mathbf{r}) \tag{1.7}$$

where M and N are amplitude vectors with complex-valued Cartesian components; k is the wavevector; and $\mathbf{r} = x\hat{\mathbf{u}}_x + y\hat{\mathbf{u}}_y + z\hat{\mathbf{u}}_z$ is the position vector expressed in the Cartesian coordinate system.

Therefore, field phasors in the metal half-space can be written as

$$\tilde{\mathbf{E}}_m(r) = \boldsymbol{M}_m \exp(i\boldsymbol{k}_m \cdot \boldsymbol{r}) \qquad (1.8)$$

$$\tilde{\mathbf{H}}_m(r) = \boldsymbol{N}_m \exp(i\boldsymbol{k}_m \cdot \boldsymbol{r}) \qquad (1.9)$$

and the field phasors in the dielectric half-space can be written as

$$\tilde{\mathbf{E}}_d(r) = \boldsymbol{M}_d \exp(i\boldsymbol{k}_d \cdot \boldsymbol{r}) \qquad (1.10)$$

$$\tilde{\mathbf{H}}_d(r) = \boldsymbol{N}_d \exp(i\boldsymbol{k}_d \cdot \boldsymbol{r}). \qquad (1.11)$$

The wave vectors $\mathbf{k}_d$ and $\mathbf{k}_m$ are already explained in Eqs. (1.1) and (1.2). In order to determine the field phasors of the SPP wave, the parameters for the SPP wave $\boldsymbol{M}_m$, $\boldsymbol{N}_m$, $\boldsymbol{M}_d$ and $\boldsymbol{N}_d$ must be determined.

Introducing Eqs. (1.8)-(1.11) into Eqs. (1.4) [Polo *et al.* (2013)]

$$\alpha_m^2 = k_0^2 \tilde{\varepsilon}_m - q^2, \qquad (1.12)$$

$$\alpha_d^2 = k_0^2 \tilde{\varepsilon}_d - q^2, \qquad (1.13)$$

where $k_0 = \omega / c_0$ is the free-space wavenumber and c_0 is the speed of light. The values obtained from Eqs. (1.12) and (1.13) must satisfy Eqs. (1.3).

In optics literature, solutions of Eqs. (1.4) can generally be classified into s-polarized (the electric field **E** parallel to the interface) and p-polarized (the magnetic field **H** parallel to the interface) electromagnetic modes. In radio-frequency literature, s-polarized modes are called transverse-electric (TE) modes, and p-polarized modes are called transverse-magnetic (TM) modes. The conditions for the SPP wave confinenment i.e. Eq. (1.2) does not fullfilled for s-polarised wave. Therefore, the SPP wave guided by the interface of two linear, homogeneous, isotropic, non-magnetic, achiral materials has to be p-polarized [Maier (2007), Polo *et al.* (2013)]. Therefore, after choosing the x-axis as the propagating direction (see Fig. 1.4), the field phasors in the metal half-space $z < 0$ may be written as [Polo *et al.* (2013)]

$$\tilde{\mathbf{E}}_m(r) = a_p \left(\frac{\alpha_m \hat{\mathbf{u}}_x + q\,\hat{\mathbf{u}}_z}{k_0 \tilde{n}_m} \right) \exp(i\boldsymbol{k}_m \cdot \boldsymbol{r}), \qquad (1.14)$$

$$\tilde{\mathbf{H}}_m(r) = -a_p \frac{\tilde{n}_m}{\eta_0} \hat{\mathbf{u}}_y \exp(i\mathbf{k}_m \cdot \mathbf{r}). \tag{1.15}$$

Similarly, the field phasors in dielectric half-space $z > 0$ may be written as

$$\tilde{\mathbf{E}}_d(r) = b_p \left(\frac{-\alpha_d \hat{\mathbf{u}}_x + q\hat{\mathbf{u}}_z}{k_0 \tilde{n}_d} \right) \exp(i\mathbf{k}_m \cdot \mathbf{r}), \tag{1.16}$$

$$\tilde{\mathbf{H}}_d(r) = -b_p \frac{\tilde{n}_d}{\eta_0} \hat{\mathbf{u}}_y \exp(i\mathbf{k}_m \cdot \mathbf{r}). \tag{1.17}$$

In these equations, a_p and b_p denote the field amplitudes in the metal and dielectric half-spaces, respectively; $\tilde{n}_m = \sqrt{\tilde{\varepsilon}_m}$ and $\tilde{n}_d = \sqrt{\tilde{\varepsilon}_d}$ are the refractive indexes of metal and the dielectric material, respectively; and $\eta_0 = \sqrt{\mu_0 / \varepsilon_0}$ is the intrinsic impedance of free space.

For the tangential component of the electric field to be continuous across the interface $z = 0$, Eqs. (1.14) and (1.16) yield [Polo *et al.* (2013)]

$$a_p \frac{\alpha_m}{\tilde{n}_m} = -b_p \frac{\alpha_d}{\tilde{n}_d} , \tag{1.18}$$

and for the tangential component of the magnetic field to be continuous across the same interface, Eqs. (1.15) and (1.17) give

$$a_p \tilde{n}_m = b_p \tilde{n}_d . \tag{1.19}$$

Equations (1.18) and (1.19) together yield the condition

$$\alpha_m \tilde{n}_d^2 + \alpha_d \tilde{n}_m^2 = 0 , \tag{1.20}$$

with $b_p = a_p \dfrac{\tilde{n}_m}{\tilde{n}_d}$. The field phasors for the SPP wave then are

$$
\left.
\begin{aligned}
\tilde{\mathbf{E}}_m(r) &= a_p \left(\frac{\alpha_m \hat{\mathbf{u}}_x + q\hat{\mathbf{u}}_z}{k_0 \tilde{n}_m} \right) \exp(i\boldsymbol{k}_m \cdot \boldsymbol{r}), \\
\tilde{\mathbf{H}}_m(r) &= -a_p \frac{\tilde{n}_m}{\eta_0} \hat{\mathbf{u}}_y \exp(i\boldsymbol{k}_m \cdot \boldsymbol{r}) \\
\tilde{\mathbf{E}}_d(r) &= a_p \frac{\tilde{n}_m}{\tilde{n}_d} \left(\frac{-\alpha_d \hat{\mathbf{u}}_x + q\hat{\mathbf{u}}_z}{k_0 \tilde{n}_d} \right) \exp(i\boldsymbol{k}_m \cdot \boldsymbol{r}), \\
\tilde{\mathbf{H}}_d(r) &= -a_p \frac{\tilde{n}_m}{\eta_0} \hat{\mathbf{u}}_y \exp(i\boldsymbol{k}_m \cdot \boldsymbol{r})
\end{aligned}
\right\} .
\tag{1.21}
$$

Using Eqs. (1.12), (1.13), and (1.20),

$$
\alpha_m^2 = \frac{k_0^2 \varepsilon_m^2}{\varepsilon_m + \varepsilon_d}
\tag{1.22}
$$

and

$$
\alpha_d^2 = \frac{k_0^2 \varepsilon_d^2}{\varepsilon_m + \varepsilon_d} \quad ,
\tag{1.23}
$$

where α_m and α_d must be chosen to satisfy Eqs. (1.3). Here, ε_m and ε_d are taken as complex quantities. Combining Eqs. (1.12) and (1.22), the dispersion relation of the SPP wave is

$$
q = k_0 \sqrt{\frac{\tilde{\varepsilon}_m \tilde{\varepsilon}_d}{\tilde{\varepsilon}_m + \tilde{\varepsilon}_d}} \quad .
\tag{1.24}
$$

The properties of the SPP wave can be examined by dispersion relation. Let us choose bulk silver as a metal whose relative permittivity is characterized by the Drude model (details are provided in Sec. 1.4.2) and air ($\tilde{\varepsilon}_d = 1$) as a dielectric material. Figure 1.5 shows the real and imaginary parts of the wavenumber q of the SPP wave as a function of ω.

The curve of Re(q) which lies to the right side of the light line is characteristic of a non-radiative SPP wave because Re(q) then exceeds the wavenumber k_0 in air. Therefore, the SPP wave can not be excited by direct illumination, and special phase matching techniques such as grating or prism coupling [Hooper and Sambles (2002),

Homola (2006), Otto (1968), Kretschmann and Raether (1968)] are required for the

excitation of the SPP wave. For $\omega > \omega_p$, the curve of Re(q) lies to left and is characteristic

of a radiative SPP wave which is not bound to the silver/air interface. A frequency gap

exists between the radiative and non–radiative SPP waves with purely imaginary q

prohibiting propagation [Maier (2007)]. The amplitude of the Im (q) is negligibly small

for $\omega_p < \omega < 0.65\ \omega_p$. Where ω_p is the angular plasma frequency and it is described in
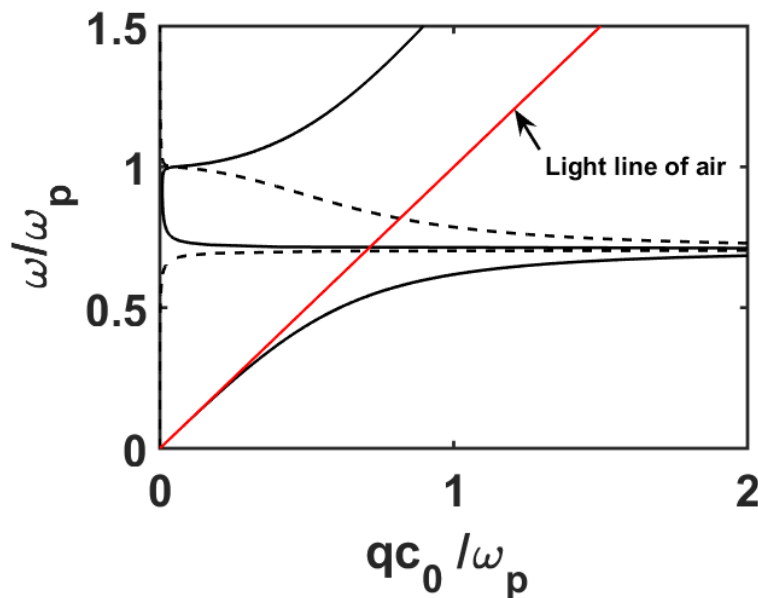
sec. 1.4.2.

Figure 1.5: The dispersion diagram of the SPP wave guided by the silver/air interface. The solid line shows the real part, and the dotted line shows the imaginary part of the wavenumber q.

1.3.2. Characteristics of SPP wave

The penetration depth, defined as the perpendicular distance in a partnering material over

which the amplitude of the electric and magnetic field reduces by a factor of $1/e$, is given

in the two partnering materials as [Polo *et al.* (2013)]

$$\Delta_d = 1/\operatorname{Im}\left(\alpha_d\right) \tag{1.25}$$

18

and

$$\Delta_{\mathrm{m}} = 1/\operatorname{Im}\left(\alpha_{\mathrm{m}}\right). \tag{1.26}$$

Generally, the penetration depths of the fields into the dielectric and the metal are around 100 nm and 10 nm, respectively in the visible spectral regime [Zia *et al.* (2006)].

The propagation distance of the SPP wave is defined as the distance along the propagation direction over which the amplitudes of the electric and magnetic fields decrease by a factor of $1/e$ and is given as [Polo *et al.* (2013)]

$$\Delta_{\mathrm{prop}} = 1/\operatorname{Im}\left(q\right). \tag{1.27}$$

The propagation distance of the SPP wave is typically in the range $10-100\ \mu\mathrm{m}$ for the silver/air interface in the visible spectral regime [Barnes *et al.* (2003)].

The phase speed of the SPP wave is given as

$$v_{p} = \omega/\operatorname{Re}\left(q\right). \tag{1.28}$$

The phase speed of the SPP wave is lower than the speed of light in vacuum.

1.3.3. Excitation of SPP wave at a planar interface

Since the phase speed of the SPP wave is larger than the phase speed of a bulk plane wave in the dielectric partnering material, direct illumination of a metal/dielectric interface from the dielectric side cannot excite the SPP wave. Special phase matching techniques such as grating coupling [Hooper and Sambles (2002), Homola (2006)], prism coupling [Otto (1968), Kretschmann and Raether (1968), Polo *et al.* (2013)], near-field excitation [Hecht *et al.* (1996)], and excitation by a highly focused laser beam [Kano *et al.* (1998)] are required. The two most popular techniques, prism coupling and grating coupling, are briefly reviewed next.

1.3.3.1 Prism-Coupled Configurations

An evanescent-wave-coupling mechanism [Polo *et al.* (2013)] facilitated by total internal reflection due to a prism is commonly used to excite the SPP wave. Figure 1.7 shows two common configurations for prism coupling: (1) Turbadar-Kretschmann-Raether and (2) Turbadar-Otto configurations.

For the Turbadar-Kretschmann-Raether configuration, as shown in Fig. 1.6 (a), a thin metal film is coated on the top of a glass prism with a relative permittivity $\tilde{\varepsilon}_{prism}$ that exceeds the relative permittivity $\tilde{\varepsilon}_d$ (which is assumed to be real and positive in this section). When the metal film is illuminated through the prism at an angle of incidence θ that is greater than the critical angle for total internal reflection, a part of the light is reflected into the prism, and a part can penetrate the metal by evanescent tunnelling. If the thickness of the metal film is very small, the evanescent wave propagates through the thin metal film into the partnering dielectric material to excite the SPP wave at the other face of the thin metal film. For the SPP wave to propagate at the metal/dielectric interface, the component of the evanescent wave's wavevector parallel to the interface should be equal to that of the SPP wave.
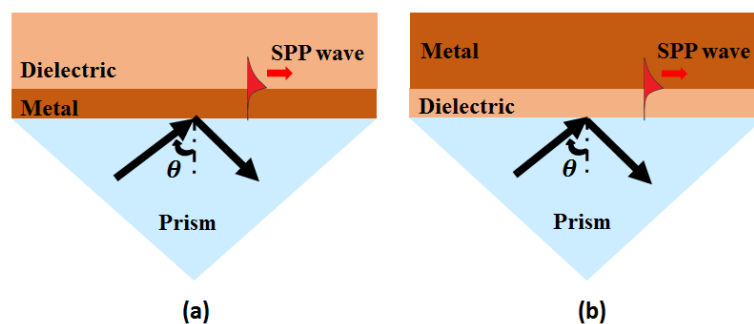

Figure 1.6: Schematics of prism-coupled configuration to excite SPP wave (a) Turbadar-Kretschmann-Raether (b) Turbadar-Otto.

The other typical configuration is the Otto configuration (Fig. 1.6 (b)), in which the prism is separated from the metal film by a thin dielectric gap. If a light wave is incident on the prism/dielectric interface at an angle of incidence θ greater than the

critical angle [Polo *et al.* (2013)] for these two media, an evanescent wave is produced at prism/dielectric interface. If the thickness of the partnering dielectric material is smaller than the decay length of the evanescent wave's field, at a certain value of θ, the component of the evanescent wave's wavevector parallel to the dielectric/metal interface is matched with the SPP wavenumber, and the SPP wave is excited.

1.3.3.2 Grating-Coupled Configuration

The SPP wave can also be excited in the grating-coupled configuration by illuminating a periodically corrugated metal grating coated with the dielectric partnering material, as shown in Fig. 1.7. The illuminated light wave is diffracted, and if the tangential component of the wavevector of a certain order of diffracted light match the SPP wavenumber, the diffracted wave can couple with the SPP wave. The grating-coupled configuration also allows the reverse process: an SPP wave propagating at a metal-dielectric interface can be radiated by the grating [Maier (2007)]. Grating coupling is currently being investigated for enhanced harvesting of solar energy in photovoltaic solar cells [Chen *et al.* (2010), Faryad and Lakhtakia (2011)].
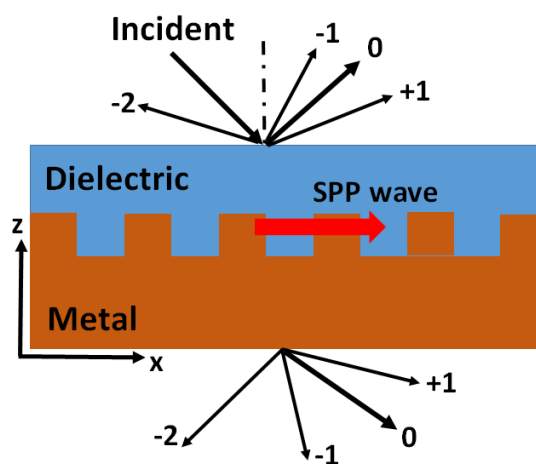

Figure 1.7: Schematic of SPP–wave excitation in the grating-coupled configuration.

1.4.   Relative-Permittivity Models for Dispersive Isotropic Materials

The models for the relative permittivity are functions of the angular frequency ω in a specific range of free-space wavelength λ_0. Each model involves parameters for the fitting of experimental data from the literature. The parameters are searched such that the difference between the experimental data and the model is minimal. The dispersive materials involved in this thesis for the propagation of the SPP waves are characterized by using well-established models such as the Lorentz, the Drude and the critical-point models.

1.4.1. Lorentz Model

The Lorentz model comes from the solution of the equation of an electron bound to a nucleus driven by an oscillating electric field $\tilde{\mathbf{E}}$. The response is equivalent to the classical mass on a spring which has damping and an external driving force. It generates damped harmonic oscillations. The complex-valued relative permittivity of an isotropic material is given as [Wooten (1972), Kittel, (1974)]

$$\tilde{\varepsilon}(\omega) = 1 + \tilde{\chi}(\omega) = 1 + \left\{ \frac{p\,\Omega}{\Omega^2\left[1+(2\pi N)^{-2}\right] - \omega^2 - i\omega\Omega/\pi N} \right\} \tag{1.29}$$

where $i = \sqrt{-1}$, $\tilde{\chi}(\omega)$ is the dielectric susceptibility, and the constants $\{p, \Omega, N\}$ represent the oscillator strength, resonance wavelength and the resonance linewidth of the material, respectively.

The Lorentz model describes radiation absorption due to inter-band transitions. These are transitions for which the electron moves to a final state corresponding to a different band without changing its wavevector in the first Brillouin zone [Wooten (1972)].

1.4.2. Drude Model

Based on the kinetic theory of electrons in a metal, the Drude model is based on the assumption that a metal has motionless positive ions and a gas of non-interacting electron. This simple model uses the classical mechanical theory of the free electron. It was constructed in order to explain the transport properties of conduction electrons in metals (due to intra-band transitions in a quantum-mechanical interpretation), conductive oxides and heavily doped semiconductors [Wooten (1972)].

Since the conduction electrons are considered to be free, the Drude oscillator is an extension of the single Lorentz oscillator to a case where the restoring force and the resonance frequency are zero. The Drude model for the relative permittivity of a metal is given as [Johnson and Christy (1972)]

$$\tilde{\varepsilon}(\omega) = 1 + \tilde{\chi}(\omega) = 1 - \left\{ \frac{\omega_p^2}{\omega(\omega + i/\tau)} \right\} \tag{1.30}$$

where $\omega_p = \sqrt{\dfrac{N_d\, q_e^2}{\varepsilon_0\, m_e}}$ is the plasma angular frequency and τ is the relaxation time. Here

$\{N_d, m_e, q_e\}$ are the density of the conduction electron, mass of electron and electronic charge, respectively. The Drude model describes well the optical properties of metals.

1.4.3. Critical-Point Model

The critical-point model was introduced in 1998 by Leng for fitting the relative permittivity of silicon [Leng *et al.* (1998)]. This model describes the interband transitions in a wide wavelength range. The critical-point model is also able to reproduce the dispersion of gold with higher accuracy [Etchegoin *et al.* (2006)]. It includes a phase factor and corresponds to first-order poles in the complex plane [Vial and Laroche (2007), Barchiesi *et al.* (2014)]. It is recommended to take two critical points terms [Etchegoin *et al.* (2006)]. The expression of the critical-point model for two critical point terms is given as [Deienga and John (2012)]

$$\tilde{\varepsilon}(\omega) = 1 + \tilde{\chi}(\omega) = 1 + \sum_{n_p=1}^{2} \tilde{\varepsilon}_{n_p}(\omega), \tag{1.31}$$

where

$$\tilde{\varepsilon}_{n_p}(\omega) = \zeta_{n_p} \frac{\Omega_{n_p}^2 + \Upsilon_{n_p}(-i\omega)}{\Omega_{n_p}^2 + 2\Gamma_{n_p}(-i\omega) - \omega^2} \tag{1.32}$$

with $\zeta_{n_p}, \Omega_{n_p}, \Upsilon_{n_p},$ and Γ_{n_p} as fitting coefficients.

1.5.   Finite-Difference Time-Domain Method

Among the more popular and widely accepted numerical methods for the solution of boundary-value problem is the finite-difference time-domain (FDTD) method [Yee (1966), Elsherbeni and Demir (2016)]. Being a time-domain technique, the FDTD methods offers several advantages for frequency-domain research since the spectral characteristics of the boundary-value problem can be obtained with a single simulation. The FDTD method can easily handle composite geometries consisting of different types of materials, including dielectric, magnetic, frequency-dependent, nonlinear, and anisotropic materials. Also, the method is easy to implement using parallel computation algorithms.
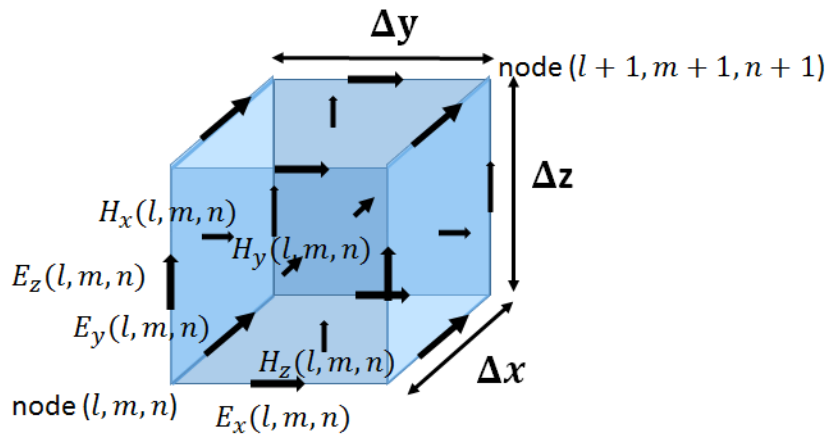

Figure 1.8: Cartesian components of the electric and magnetic field component in the YEE cell indexed as (l, m, n).

The FDTD algorithm is constructed from the time-domain Maxwell equations. The computational domain is represented by a spatial grid and the Cartesian components of the electric and the magnetic fields are computed at certain discrete positions in space at discrete instances of time. The first derivatives with respect to time and space appearing in the Maxwell equations are approximated by second-order central differences [Elsherbeni and Demir (2016)]. A set of equations to calculate the values of fields at a future time instant from the values of the fields at a past time instant are thereby obtained, leading to a marching algorithm that simulates the evolution of the fields in time.

The unit cell of the spatial grid is called a Yee cell. Rectangular Yee cells are used for a stepped approximation of the geometry with spatial resolution set by the dimensions of the unit cell. The discrete spatial positions of the field components, associated with a cell indexed as (l, m, n), have a specific arrangement in the Yee cell, as demonstrated in Fig. 1.8 (for three-dimensional geometry). Yee cells having the dimension Δx in the x-direction, Δy in the y-direction, and Δz in the z-direction. For a time-sampling period Δt, the electric field components are sampled at time instants 0, Δt, $2\Delta t$, ..., $p\Delta t$; however, the magnetic field components are sampled at time instants $\frac{1}{2}\Delta t$, $\left(1+\frac{1}{2}\right)\Delta t$, ..., $\left(p+\frac{1}{2}\right)\Delta t$. The relevant FDTD updating equations for the three-dimensional problem if the material is linear, isotropic and non-dispersive are given as [Elsherbeni and Demir (2016)]

$$H_x^{p+\frac{1}{2}}(l,m,n) = H_x^{p-\frac{1}{2}}(l,m,n) + \frac{\Delta t}{\mu_x(l,m,n)\Delta z}\Big[E_y^p(l,m,n+1) - E_y^p(l,m,n)\Big]$$
$$-\frac{\Delta t}{\mu_x(l,m,n)\Delta y}\Big[E_z^p(l,m+1,n) - E_z^p(l,m,n)\Big]$$

(1.33)

$$H_y^{p+\frac{1}{2}}(l,m,n) = H_y^{p-\frac{1}{2}}(l,m,n) + \frac{\Delta t}{\mu_y(l,m,n)\Delta x}\left[E_z^p(l+1,m,n) - E_z^p(l,m,n)\right]$$

$$- \frac{\Delta t}{\mu_y(l,m,n)\Delta z}\left[E_x^p(l,m,n+1) - E_x^p(l,m,n)\right] \tag{1.34}$$

$$H_z^{p+\frac{1}{2}}(l,m,n) = H_z^{p-\frac{1}{2}}(l,m,n) + \frac{\Delta t}{\mu_z(l,m,n)\Delta y}\left[E_x^p(l,m+1,n) - E_x^p(l,m,n)\right]$$

$$- \frac{\Delta t}{\mu_z(l,m,n)\Delta x}\left[E_y^p(l+1,m,n) - E_y^p(l,m,n)\right] \tag{1.35}$$

$$E_x^{p+1}(l,m,n) = E_x^p(l,m,n) + \frac{\Delta t}{\varepsilon_x(l,m,n)\Delta y}\left[H_z^{p+\frac{1}{2}}(l,m,n) - H_z^{p+\frac{1}{2}}(l,m-1,n)\right]$$

$$- \frac{\Delta t}{\varepsilon_x(l,m,n)\Delta z}\left[H_y^{p+\frac{1}{2}}(l,m,n) - H_y^{p+\frac{1}{2}}(l,m,n-1)\right] \tag{1.37}$$

$$E_y^{p+1}(l,m,n) = E_y^p(l,m,n) + \frac{\Delta t}{\varepsilon_y(l,m,n)\Delta z}\left[H_x^{p+\frac{1}{2}}(l,m,n) - H_x^{p+\frac{1}{2}}(l,m,n-1)\right]$$

$$- \frac{\Delta t}{\varepsilon_y(l,m,n)\Delta x}\left[H_z^{p+\frac{1}{2}}(l,m,n) - H_z^{p+\frac{1}{2}}(l-1,m,n)\right] \tag{1.36}$$

$$E_z^{p+1}(l,m,n) = E_z^p(l,m,n) - \frac{\Delta t}{\varepsilon_z(l,m,n)\Delta y}\left[H_x^{p+\frac{1}{2}}(l,m,n) - H_x^{p+\frac{1}{2}}(l,m-1,n)\right]$$

$$+ \frac{\Delta t}{\varepsilon_z(l,m,n)\Delta x}\left[H_y^{p+\frac{1}{2}}(l,m,n) - H_y^{p+\frac{1}{2}}(l-1,m,n)\right]. \tag{1.37}$$

Where, $E_x, E_y, E_z, \varepsilon_x, \varepsilon_y,$ and ε_z are the electric field components and permittivity of the material in x, y, and z-direction, respectively. Similarly, $H_x, H_y, H_z, \mu_x, \mu_y,$ and μ_z are the magnetic field components and permeability of the material in x, y, and z-direction, respectively.

In order to avoid instability in the simulation, space and time intervals must satisfy the Courant-Friedrichs-Lewy condition [Yee (1966), Elsherbeni and Demir (2016)]

$$c_0 \Delta t \sqrt{\left(\frac{1}{\Delta x}\right)^2 + \left(\frac{1}{\Delta y}\right)^2 + \left(\frac{1}{\Delta z}\right)^2} \le 1 . \tag{1.38}$$

The time-marching algorithm of the FDTD method is illustrated in Fig. 1.9. The first step in this algorithm is setting up the computational domain (including objects and the material those objects are made of) and the field sources. The field components need to be defined as arrays as well. The latter arrays are initialized with zeros, since the initial values of the fields are zeros and non-zero values are to introduced as the simulation proceeds. At every step of the time-marching iteration, the components of the magnetic field are updated for time instant $(p + 0.5)\Delta t$. Then the components of the electric field are updated for time instant $(p + 1)\Delta t$. As the computational domain has a finite size in space, specific boundary conditions such as absorbing boundary conditions [Berenger (1994)] have to be enforced on the spatial boundaries of the computational domain. After the fields are updated and boundary conditions are enforced, the current values of any desired field components can be captured and stored as output data, for real-time processing or post-processing to calculate some other desired parameters. The FDTD simulation is continued until some stopping criteria are satisfied.
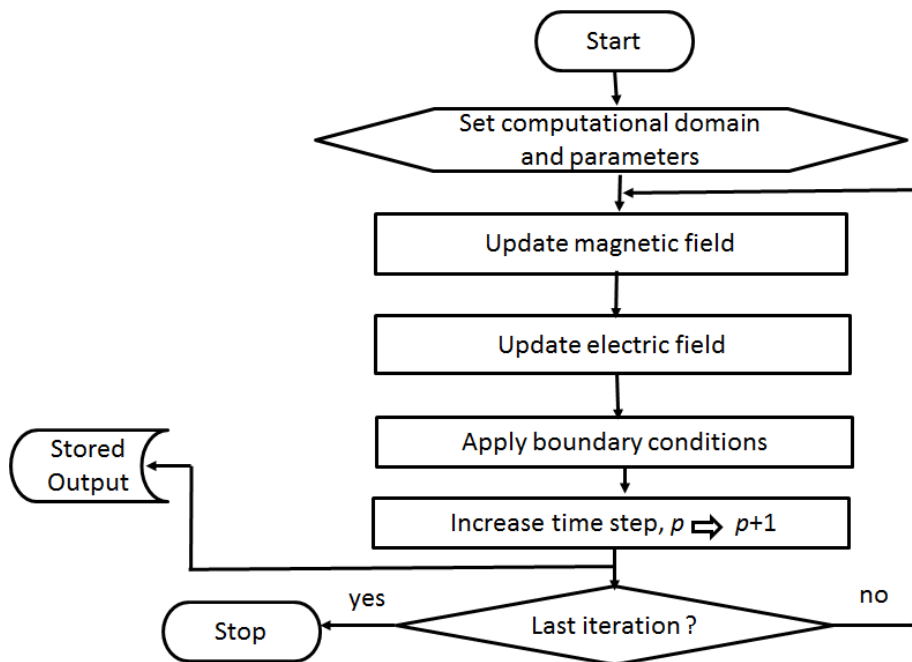

Figure 1.9: FDTD time-marching algorithm.

The FDTD method provides the approximation of the real behaviour of the field and introduces an error to the solution. The error varies with frequency, the spatial grid size, and direction of propagation of the wave. The difference of actual phase velocity and the phase velocities numerically obtained by the FDTD method is known as numerical dispersion. The temporal and spatial sampling periods Δt, Δx, Δy, and Δz are chosen sufficiently small to reduce the numerical dispersion error.

1.6.   Correlation Coefficients

In order to assess the adequacy of a communication system, a suite of received signals have to be correlated against a suit of the corresponding transmitted signals. This is done by using advanced statistical techniques which would eventually allow the determination of optimal configurations for information transfer with acceptable fidelity. For example, consider a communication system in which points labeled R and S are identified as the points of transmission and reception, respectively, as shown in Fig.1.10. The transmitting signal has any specific shape such as the Gaussian pulse shown in Fig. 1.10. The received signal consist of (1) a shifted and scaled version of the transmitted signal and (2) random noise in the form of distortions of the shape and duration resulting from the propagation of the signal in the medium. The information which is transmitted in the form of the Gaussian pulse can be successfully recovered at the reception point if the received signal's shape and duration are similar to those of the transmitted signal. The similarity between the transmitted and the received signals is assessed quantitatively using correlation coefficients.

Correlation coefficients are used in statistics to measure the strength of the relationship between two quantities that vary in relation to a certain parameter. Of the several types of correlation coefficients used to determine the similarity between two signals, the Pearson correlation coefficient [Rodgers and Nicewander (1988)] is perhaps

the most widely used one. In this thesis, the fidelity of the information transfer by a pulse-modulated carrier SPP wave is determined by the Pearson and the concordance correlation coefficients [Lin (1989)]. The Pearson correlation coefficient correlates the shapes and duration of two signals $x(t)$ and $y(t)$, whereas the concordance correlation coefficient correlates the agreement between the two signals.

The **Pearson correlation coefficient** $(\rho_{P_{xy}})$ is defined as [Rodgers and Nicewander (1988)]

$$\rho_{P_{xy}} = \frac{\sum_{\ell=1}^{N}(x_{\ell}-\overline{x})(y_{\ell}-\overline{y})}{\sqrt{\sum_{\ell=1}^{N}(x_{\ell}-\overline{x})^{2}}\sqrt{\sum_{\ell=1}^{N}(y_{\ell}-\overline{y})^{2}}} \tag{1.38}$$

where $x_{\ell} = x(t_{\ell}), \quad y_{\ell} = y(t_{\ell})$

$$\overline{x} = \frac{1}{N}\sum_{\ell=1}^{N}x(t_{\ell}), \tag{1.39}$$

and

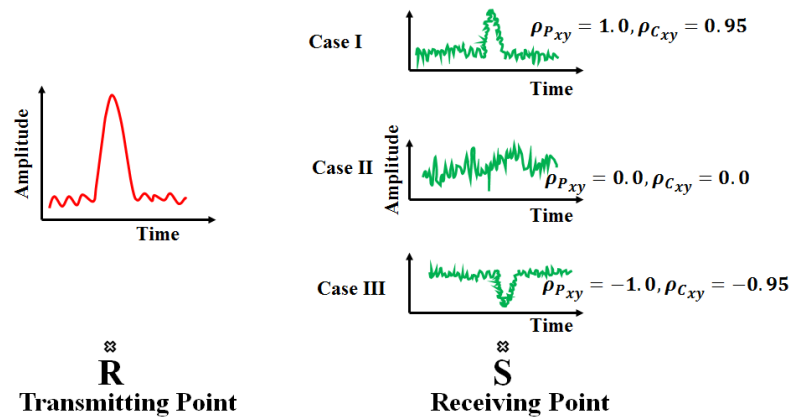$$\overline{y} = \frac{1}{N}\sum_{\ell=1}^{N}y(t_{\ell}). \tag{1.40}$$

Figure 1.10: Schematic showing the different values of correlation coefficients.

The range of $\rho_{P_{xy}}$ is [-1, 1], where

- +1 indicates a strong positive relationship (Fig. 1.10, case I),

- 0 indicates no relationship at all, (Fig. 1.10, case II) and

- -1 indicates a strong negative relationship (Fig. 1.10, case III).

The **concordance correlation coefficient** is defined as [Lin (1989)]

$$\rho_{C_{xy}} = \rho_{P_{xy}} C_b \qquad (1.41)$$

where the bias factor

$$C_b = \frac{2}{\left(\dfrac{\sigma_x}{\sigma_y}\right) + \left(\dfrac{\sigma_y}{\sigma_x}\right) + \dfrac{(\bar{x} - \bar{y})^2}{\sigma_x \sigma_y}}, \qquad (1.42)$$

$$\sigma_x = \sqrt{\frac{1}{N} \sum_{\ell=1}^{N} \left[x(t_\ell) - \bar{x} \right]^2}, \qquad (1.43)$$

and

$$\sigma_y = \sqrt{\frac{1}{N} \sum_{\ell=1}^{N} \left[y(t_\ell) - \bar{y} \right]^2}. \qquad (1.44)$$

Since C_b is [0, 1] and $\rho_{P_{xy}} \in [-1, 1]$, it follows that $\rho_{C_{xy}} \in [-1, 1]$. In general, the concordance correlation coefficient is less than the Pearson correlation coefficient [Liao *et al.* (2016)]. The closer that $\left| \rho_{C_{xy}} \right|$ is to unity, the stronger is the correlation or anticorrelation, as indicated by the sign of $\rho_{C_{xy}}$. If $y(t)$ is independent of the $x(t)$, then $\rho_{C_{xy}} = 0$.

1.7.   Literature Review

Electromagnetic surface waves are investigated widely by researchers. Excellent introductions to ESWs and SPP waves can be found in various books [Polo *et al.* (2013), Maier (2007)] and numerous review papers [Pitarke *et al.* (2007), Barnes *et al.* (2003), Zayats *et al.* (2005), Zia *at al.* (2006)]. The pioneer experimental setups for facile excitation of SPP waves were introduced by Otto [Otto (1968)] and Kretschmann and Raether [Kretschmann and Raether (1968)].

In 1903, the existence of an electromagnetic surface wave guided by the planar interface of air/seawater was theoretically established [Uller (1903)]. Four years later, a similar theoretical study of electromagnetic wave propagation on the planar interface of air and ground in the microwave regime was proposed by Zenneck [Zenneck (1907)]. In 1909, Sommerfeld further mathematically analyzed the electromagnetic wave propagation on the interface two different material [Sommerfeld (1909)] which is now known as the Zenneck wave [Hill and Wait (1980)]. In 1949, Bohm described plasma oscillations in metals exposed to electric fields [Bohm and Gross (1949)a, Bohm and Gross (1949)b]. Pierce observed the oscillations of ionic plasmas in vacuum tubes [Pierce (1949)]. The quantum of plasma oscillations is a quasiparticle dubbed the plasmon [Pines (1956)]. A few years later, the energy losses of electrons impinging on a metal film were explained in terms of electronic-plasma oscillations occurring at the film's surfaces [Ritchie (1957)]. Two years later, in a series of electron energy-loss experiments Powell and Swan [Powell and Swan (1959)a, Powell and Swan (1959)b] demonstrated the existence of these collective excitations, the quanta of which Stern and Ferrell called the surface plasmon [Stern and Ferrell (1960)].

Since then, there has been a significant advance in both theoretical and experimental investigations of surface plasmons. Classically, a train of surface plasmons is called a surface-plasmon wave. When the metal has a boundary with a dielectric material, the term surface-plasmon-polariton wave is used, as explained in Sec. 1.3. SPP waves have been employed in wide spectrum of applications such as optical biosensing [Nylander et al. (1982), Malmqvist (1993), Chien and Chenb (2004)], surface-plasmon resonance technology [Gordon and Ernst (1980), Schuster et al. (1993), Homola et al. (1999), Green et al. (2000)], scanning tunnelling microscopy [Berndt and Gimzewski

(1991)], and surface-plasmon microscopy [Rothenhausler and Knoll (1988), Flatgen *et al.* (1995)].

Renewed interest in SPP waves has come from recent advances in the investigation of the electromagnetic properties of nanostructured materials [Pendry (1999)]. In order to enhance optical transmission, light is concentrated and channelled through a periodic arrays of holes in a dielectric slab [Leuthold *et al.* (2010), Chuttinan and Noda (2000)]. However, due to the diffraction limit, the size of the optical waveguide (dielectric photonics waveguide) is several wavelengths long. Hence a huge size mismatch between the large-scale of integrated photonics and the small scale of integrated electronics occurs [Leuthold *et al.* (2013), Sekhon and Verma (2011)].

The most attractive aspects of the SPP wave is that its fields are concentrated on the subwavelength length scale [Barnes *et al.* (2003)]. Thus, SPP-wave-based optical interconnects may overcome the limitations of the electronic and optical interconnects and can be used to transmit the information inside a microelectronic chip. SPP-wave-based optical modulators and switches have also been successfully investigated [Krasavin and Zheludev (2004), Haffner *et al.* (2015)].

The research on SPP-wave-based circuits has made major advances in the past few years. Many researchers provided a perspective and possibilities of merging the electronics and photonics at the nanoscale by SPP wave [Brongersma *et al.* (2007), Schuller *et al.* (2010)]. In 2007, Conway compared electronic and SPP-wave-based interconnects and showed that latter offer higher interconnect density, shorter signal delay, and less cross talk compared to the former [Conway *et al.* (2007)]. In 2008, Kim demonstrated a chip–to–chip optical interconnect that exploits long-range SPP wave propagation [Kim *et al.* 2008].

SPP wave propagation along a continuous planar dielectric/metal interface is heavily investigated using Maxwell equations in the frequency domain [Abdulhalim *et al.* (2008), Maier (2007), Polo *et al.* (2013), Homola (2006)]. Very few papers on the scattering of an SPP wave by a discontinuity are available [Novitsky (2010), Foley *et al.* (2014)]. Recently Armin *et al.* investigated the SPP wave propagating on a surface discontinuity [Armin *et al.* (2018)].

1.8.   Research Objective

The objective of the research undertaken for this thesis is to investigate the propagation and scattering of pulse-modulated carrier SPP waves in the time-domain in an environment that represents an interconnect such as may be encountered in an IC. The motivation for investigating the transport of information using SPP waves is to overcome the limitations of electronic interconnects in a semiconductor chip.

The research tasks carried out for this thesis are as follows:

(i)   Analysis of the effect of the carrier frequency on information transmission, as the constitutive properties of materials are frequency-dependent, in general.

(ii)   Comparison of the shapes and durations of the transmitted and received pulses,

(iii)   Determination of the effects of choosing different materials on information transmission.

1.9.   Organization of the Thesis

In Chapter 2, information carried by a SPP wave across a semi-infinite gap on the metallic side of a planar metal/dielectric interface is numerically investigated in the time-domain. The Drude model is used for the relative permittivity of the metal and air is taken as the dielectric material. The FDTD method is used to compute the evolution of the

electromagnetic fields everywhere in a computational domain encompassing the guiding interface as well as the gap. The pulse-modulated carrier SPP wave is launched in the computational domain by applying the initial fields and proper boundary conditions to the launching plane. Due to the different spectral components of the signal having different phase speeds, the temporal profile of the signal broadens as it moves in the forward direction and amplitude reduction occurs due to the dissipation of electromagnetic energy in the metal. Information transfer by SPP wave is investigated: (1) for the abrupt termination of the metal to determine the characteristics of the launched signal and (2) when the metal is restored after the gap of width equal to the carrier wavelength in free space. The Pearson correlation coefficient of the forward-directed component of the Poynting vector at two points on either side of the gap is calculated. The received signal is found to be strongly and positively correlated with the transmitted signal, a promising result for information transfer through SPP-wave-based optical interconnects.

In Chapter 3, transfer of information via a pulse-modulated carrier SPP wave around a concave corner formed by two planar metal/air interfaces is presented. The signal is launched along the first metal/air interface and received along the second metal/air interface. The effects of the corner angle and carrier wavelength on information transmission are investigated. The dependency of the scattered field on the radial distance from the corner is also examined for two different corner angles. The signal received after traversing the concave corner is strongly and positively correlated with the transmitted signal.

In Chapter 4, transport of information by a carrier SPP wave guided by a planar silicon/silver interface in the near-infrared spectral regime is presented. The pulse-modulated carrier SPP wave encounters an upright wall between silicon and air or silicon

34

and silver. The transmission of the signal beyond this wall is simulated to determine the fidelity of information transfer beyond the wall, as assessed using the Pearson and the concordance correlation coefficients. Information can be transferred across a few tens of micrometers, which amounts to more than 600 transistors laid end-to-end in 14-nm technology chips.

In Chapter 5, the research presented in the thesis is summarized. The major conclusions emanating from the research and their significance are highlighted. Finally, some lines of investigation for future research suggested.

Appendix A describes the perfectly matched layer (PML) bordering the computational domain to prevent reflection back into the computation domain. The details of the incorporation of the PML in the FDTD method are presented.

Appendix B includes the MATLAB programs that can be used to obtain the numerical results presented in Chapters 2, 3, and 4.